Nano Research

Open Access

Research Article

Three-dimensional lightweight melamine foams modified by MXene sheets and CoNi alloys towards multifunctional microwave absorption

Nannan Wu[1,§]✉, Zhengying Shen[1,§], Yitao Ma[1], Zhizheng Wu[2], Chuanxin Hou[3]✉, Sijie Guo[4], Jian Tian[1]✉, and Jiurong Liu[5]✉

[1] *School of Material Science and Engineering, Shandong University of Science and Technology, Qingdao 266590, China*
[2] *School of Mathematics and Systems Science, Shandong University of Science and Technology, Qingdao 266590, China*
[3] *School of Environmental and Material Engineering, Yantai University, Yantai 264005, China*
[4] *Department of Chemical & Biomolecular Engineering, University of Tennessee, Knoxville, TN 37996, USA*
[5] *Key Laboratory for Liquid-Solid Structural Evolution and Processing of Materials, Ministry of Education and School of Materials Science and Engineering, Shandong University, Jinan 250061, China*
[§] *Nannan Wu and Zhengying Shen contributed equally to this work.*

Cite this article: *Nano Research*, **2025**, *18*, 94907121. https://doi.org/10.26599/NR.2025.94907121

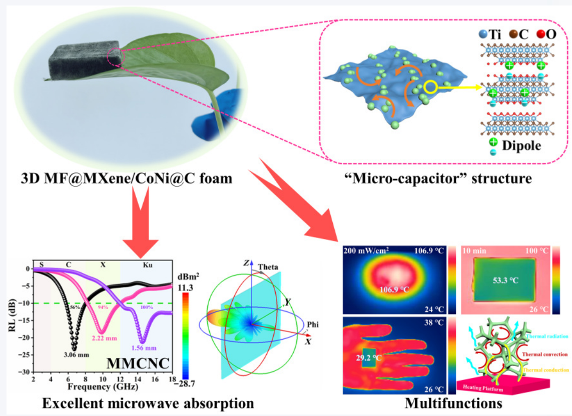

ABSTRACT: Taking the increasing issue of electromagnetic waves (EMW) pollution and the necessity for applications in extreme environments, there is a pressing requirement to create multifunctional microwave absorption materials (MAMs) to meet the current challenges. In this work, we achieved the successful combination of MXene sheets and metal organic framework (MOFs) derived CoNi@C magnetic alloys onto the three-dimensional (3D) melamine foam (MF) skeleton using vacuum impregnation and electrostatic self-assembly techniques. The obtained MF@MXene/CoNi@C composite foams achieved outstanding MA performance, with an optimal reflection loss (RL) value of –24.1 dB and a maximum effective absorption bandwidth (EAB) of 6.88 GHz at a thickness of 1.68 mm, effectively covering the whole Ku band. The superior MA performance is ascribed to the composite foams' multi-component architecture, distinctive 3D porous structure, and the synergistic impact of multiple loss mechanisms. Moreover, the MF@MXene/CoNi@C composite foams demonstrate exceptional photothermal conversion, thermal insulation, and infrared stealth capabilities, effectively coping with the demands of applications in extreme environments. This work serves as a valuable resource and source of inspiration for the development of lightweight-broadband, multifunctional efficient MAMs.

KEYWORDS: multifunctional, microwave absorption, MXene, thermal insulation, infrared stealth

1 Introduction

In this intelligent era of electronic information explosion, electromagnetic waves (EMW) are ubiquitous, and like invisible messengers, they carry rich information and play a pivotal role in wireless communication, radar detection, medical equipment, and other fields [1–3]. Nevertheless, with the wide application of various electronic devices, the EMW radiation has become increasingly prominent, which has a far-reaching impact on human life and military security [4–6]. The EMW interference not only reduces communication quality, but also poses possible harm to human health, electronic equipment, and the environment [7–9]. Therefore, the development of high-efficiency and broad-band microwave absorption (MA) materials (MAMs) has become a common concern of the current scientific and technological community [10, 11].

In general, the MA performance of the material is closely related

Received: September 1, 2024; **Revised:** October 25, 2024
Accepted: November 7, 2024

✉Address correspondence to Nannan Wu, skd996364@sdust.edu.cn; Chuanxin Hou, chuanxin210@ytu.edu.cn; Jian Tian, jiantian@sdust.edu.cn; Jiurong Liu, jrliu@sdu.edu.cn

to its composition and microstructures [12–15]. Therefore, composites with multicomponent and unique structural designs will be the focus of future research on efficient MAMs. Currently, among the various kinds of MAMs, two-dimensional materials such as MXene [16, 17], graphene [18, 19], and MoS_2 [20, 21] are considered as the most promising candidates. Among them, MXene, as an emerging two-dimensional (2D) transition metal carbide material, has demonstrated significant benefits in fields of EM protection due to its abundant surface functional groups, stable spatial structure, large specific surface area, and good electrical conductivity [3, 22–24]. Nevertheless, pure MXene material will lead to problems such as impedance mismatch and single loss mechanism, limiting its effect in practical applications [25, 26]. Researchers typically compound it with magnetic loss materials to achieve dielectric/magnetic loss synergy and in turn improve the impedance matching of materials. For instance, Pan et al. reported the synthesis of multilayer sandwiched MXene heterostructure modified with one-dimensional Co nano-chains and achieved an optimal reflection loss (RL) of –46.48 dB at 16.75 GHz [27]. Li's team [28] prepared MXene/Ni composites by combining Ni particles with MXene via electrostatic self-assembly, with a maximum RL of –50.5 dB and an effective absorption bandwidth (EAB) of 5.28 GHz at a thickness of 3.5 mm.

Nevertheless, the composite of MXene and magnetic materials also faces nonnegligible challenges, such as the large density and the self-stacking of MXene sheet layers [29]. To overcome these problems, melamine foam (MF) can be used as an ideal matrix for carrying MXene and magnetic nanoparticles due to its high open porosity, lightweight, and three-dimensional (3D) skeletal structure. Jia and co-workers [30] made 3D composite foams by applying one-dimensional Co_3O_4 and two-dimensional MXene onto the MF skeleton through vacuum impregnation and an electrostatic self-assembly process. Due to the synergistic effect of the multi-reflections from porous structure and dielectric/magnetic loss, the composite foams have exceptional MA performance with the best RL value of –51.31 dB and EAB of 6.96 GHz at 2.3 mm. Cheng et al. [26] successfully assembled Ni magnetic particle-anchored reduced graphene oxide (RGO)/MXene on MF via an electrostatic self-assembly and hydrazine vapor reduction process, which showed a minimum RL value of –61.3 dB and EAB of 7.04 GHz. Apart from possessing high-performance MA, the advanced MAMs should take into various functions, such as excellent compressibility, thermal insulation, and photothermal conversion, to fulfill the requirements of complex and changing environments [31–33]. The high porosity and low thermal conductivity of MF are beneficial to reduce heat transfer, and protect electronic devices or the human body from high temperatures [34, 35]. Moreover, the superior thermal insulation performance also exhibits potential infrared stealth capability to protect devices from radar detection [36, 37]. In addition, MXene's local surface plasmon resonance (LSPR) effect renders it an exceptional candidate for photothermal applications. Therefore, assembling MXene and magnetic nanoparticles on 3D MF is an effective strategy to achieve high-performance MAMs with multifunction.

Herein, we successfully assembled the composite foams with MXene sheets and CoNi magnetic particles on surface of MF skeleton (MF@MXene/CoNi@C) via vacuum impregnation and electrostatic self-assembly processes. The distinctive 3D porous architecture of the composite foams reduced the agglomeration of MXene sheets and possessed lightweight features. The multi-component design and the multiple loss mechanisms result in the optimal RL value of MF@MXene/CoNi@C being –24.1dB and the EAB reaching 6.88 GHz at 1.68 mm, covering the entire Ku band. Benefiting from the perfect impedance matching and strong attenuation capabilities, the composite foams exhibit exceptional MA performance. In addition, MF@MXene/CoNi@C achieves multi-functionalization in terms of photothermal conversion, thermal insulation, and infrared stealth, which is promising for a wide range of applications in aerospace, military stealth, and electronic devices. This work provides an effective strategy for the development of multi-functional MAMs.

2 Experimental

2.1 Preparation of $Ti_3C_2T_x$ MXene and CoNi@C

The few-layered $Ti_3C_2T_x$ MXene was obtained by adopting *in-situ* etching method in the HCl/LiF mixture. Typically, 3.2 g LiF was dissolved into HCl solution (9 M). Then 2 g Ti_3AlC_2 was added into the above solution and stirred for 24 h at 35 °C. After repeated centrifugation until the pH value reached 6, the precipitate was collected and then redispersed in deionized water. The $Ti_3C_2T_X$ MXene solution was obtained after sonication and centrifugation for another 1 h. The CoNi@C was prepared by using metal-organic frameworks as the template. In a typical synthesis procedure, 0.873 g of nickel nitrate hexahydrate ($Ni(NO_3)_2{\cdot}6H_2O$) and 0.873 g of cobalt nitrate hexahydrate ($Co(NO_3)_2{\cdot}6H_2O$) were dissolved in 30 mL of methanol to create solution A. Solution B was formed by dissolving 1.97 g of di-methyl imidazole (2-MI) in another 20 mL of methanol. Solution B was added dropwise to solution A, stirred continuously for 10 h at room temperature, and then allowed to stand for 2 h. The mauve-colored CoNi-MOFs precursors were collected by centrifugal washing with methanol several times. Finally, the CoNi-MOFs precursor was calcined at 700 °C under an Ar atmosphere for 4 h to obtain the CoNi@C composite, named CNC.

2.2 Preparation of MF@MXene/CoNi@C

The MF@MXene/CoNi@C was prepared via vacuum impregnation and electrostatic self-assembly procedures. During the synthesis process, the MF was first ultrasonically treated with ethanol and deionized water for 30 min each, followed by multiple washes with deionized water and drying. The treated MF was thoroughly impregnated in a monolayer of MXene solution (5 mg/mL) for 2 h and dried to obtain the MF@MXene composite. Subsequently, 0.3 g of CoNi@C was ultrasonically dissolved in hexadecyl trimethyl ammonium bromide (CTAB) solution (2 mg/mL) for 30 min before being dried and stored. Finally, MF@MXene was impregnated in CoNi@C (CTAB) solution (20 mg/mL) for 2 h to allow complete electrostatic adsorption and dried to obtain MF@MXene/CoNi@C. The obtained MF@MXene and MF@MXene/CoNi@C composites were defined as MM and MMCNC, respectively.

2.3 Characterizations

X-ray diffractometer (XRD, Japan SmartLab SE), Raman spectroscopy (DXR2), scanning electron microscopyy (SEM, Czech TESCAN MIRA LMS), transmission electron microscopy (TEM, Japan JEOL-JEM-2100F), and X-ray photoelectron spectroscopy (XPS, America Thermo Scientific K-Alpha) were used to analyze the composition, microscopic morphology, and chemical valence states of the materials. The functional groups and vacancy defects of the samples were evaluated by Fourier Transform Infrared Spectroscopy (FTIR, IRTracer 100) and electron paramagnetic resonance (EPR, Bruker EMXplus-6/1), respectively. The vibrating sample magnetometer (VSM, America LakeShore 7404) was measured for the magnetic capabilities of the materials. 808 nm Near Infrared Laser (NIL, LWIRPD-5F), Infrared Thermal Imager (ITI, FOTRIC 220S), and Thermostatic Heating Platform (THP, JF-956S) to evaluate the photothermal conversion and infrared stealth capabilities of materials. EM parameters were determined using a vector network analyzer (VNA, N5244A Agilent). The foams were mixed into and 70 wt.% paraffin homogeneously and then cut into a coaxial ring (φ_{in} = 3.04 mm, φ_{out} = 7.00 mm). During the measurement process, the analyzer was warmed up and then calibrated using standard tools. Finally, the EM parameters were calculated by the analyzer software.

3 Results and discussion

3.1 Microstructures and compositions

The detailed synthesis route for MF@MXene/CoNi@C composites is shown in Scheme 1. Firstly, magnetic spherical CoNi@C particles were prepared by *in-situ* deposition and high-temperature sintering. The obtained CoNi@C was treated with CTAB to make them positively charged. After that, the pre-treated MF was immersed in a monolayer MXene solution, and the MXene sheets adhered firmly to the MF surface, which could be proved by the Video S1 in the Electronic Supplementary Material (ESM). Finally, CoNi@C (CTAB) is adsorbed on the surface of MF@MXene by electrostatic self-assembly to obtain MF@MXene/CoNi@C.

The XRD patterns revealed all samples' phase compositions and crystal structures, as illustrated in Fig. 1(a) and Fig. S1(a) in the ESM. In the pattern of Fig. 1(a), the broad and weak peak at 23.68° was observed as MF. In Fig. S1(a) in the ESM, the peaks representing (104) crystal planes of Ti_3AlC_2 disappeared and the peak of (002) crystal plane has shifted from 9.5° to 6.2°, indicating the successful exfoliation of $Ti_3C_2T_x$ MXene. The SEM and TEM images of delaminated MXene sheets are presented in Figs. S1(b) and S1(c) in the ESM, which showed the MXene sheets possessed monolayer structure with lateral dimension of 0.5–1.0 μm. When immersing MF into MXene solution, the appearance of (002) diffraction peak for MM indicates the existence of the MXene sheets (Fig. 1(a)). The connection between MF foam and MXene sheets should be mainly attributed to the presence of hydrogen bonds, which could be revealed through variations of stretching vibration frequency or intensity in FTIR [38]. The FTIR test in Fig. S2(a) in the ESM showed the N–H absorption peak at 3308 cm^{-1} of MF was significantly decreased, which was attributed to the formation of hydrogen bonding between the amide group of MF and oxygen-containing groups (Ti–O, etc.) of MXene [38–40]. Meanwhile, the presence of Ti–O bond for MM proved the MXene was successfully incorporated into MF skeleton. After further electrostatic assembling with CoNi particles, the three diffraction peaks of MMCNC at 44.48°, 51.69°, and 76.17° corresponded exactly to the (111), (200), and (220) crystal planes of Co (JCPDS NO. 15-0806) and Ni (JCPDS NO. 04-0850) for MMCNC [25, 41]. In order to further investigate the illustration of the electrostatic effect between MXene sheets and positively charged CoNi particles, the surface charges of MM, CNC, and MMCNC were characterized by zeta potential analyzer. The results of Fig. S1(d) in the ESM showed that the zeta potentials of MM, CNC, and MMCNC are −24.3, 13.3, and −0.286 mV, respectively. Thus the positively charged CNC could be adsorbed to surface of MM with negative charges, which further confirms the successful preparation of MF@MXene/CoNi@C composite. Figure 1(b) displays the Raman spectra of the samples, where D and G bands near 1370 and 1560 cm^{-1} could be observed for sample CNC, indicating the formation of carbon derived from the decomposition of MOFs precursor. In addition, the Raman spectra of MM and MMCNC exhibit prominent peaks at 151.2, 372.9, and 630.4 cm^{-1}, which align with the distinctive peaks of monolayer $Ti_3C_2T_x$ MXene [42]. The introduction of monolayer MXene can significantly affect the conductive properties and provide abundant sites for deposition of magnetic particles.

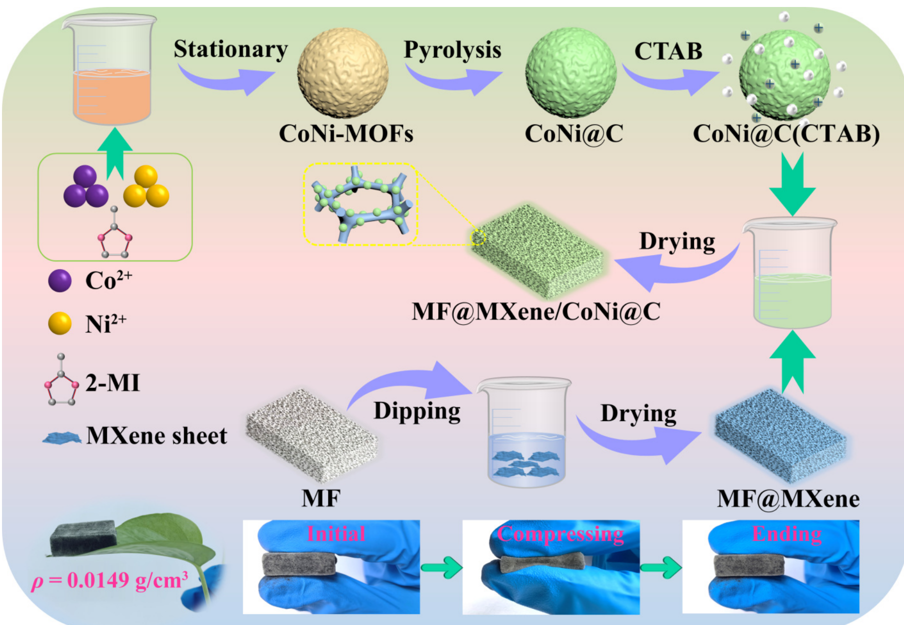

Scheme 1 Diagram for the preparation of MF@MXene/CoNi@C composite.

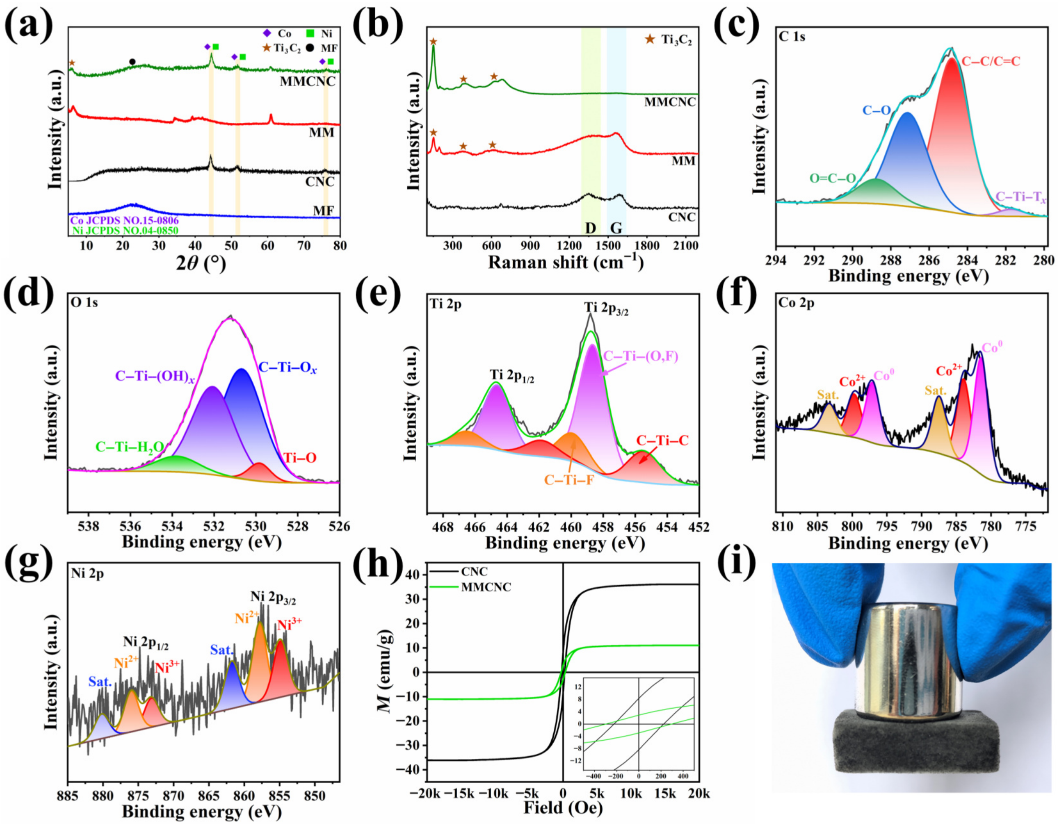

Figure 1 (a) XRD pattern and (b) Raman spectrum of samples. (c)–(g) XPS spectra of MMCNC. (h) VSM curves of CNC and MMCNC. (i) Magnetism of MMCNC.

To determine the chemical valence states of the composites, the XPS spectra of MMCNC are shown in Figs. 1(c)–1(g) and Fig. S2(b) in the ESM. The XPS survey spectrum displays characteristic peaks for the elements C, O, F, Ti, Co, and Ni (Fig. S2(b) in the ESM). In the C 1s spectrum (Fig. 1(c)), the peaks at 281.72, 284.8, 287.12, and 288.76 eV represent C–Ti–T_x, C–C/C=C, C–O, and O=C–O groups, respectively [26, 43]. As shown in Fig. 1(d), the peaks at 529.82, 530.67, 532.06, and 533.79 eV in the O 1s curves belong to Ti–O, C–Ti–O_x, C–Ti–$(OH)_x$ and C–Ti–H_2O bonds, respectively [29]. The Ti 2p curves were fitted to the three pairs of peaks, C–Ti–C (455.26 and 461.66 eV), C–Ti–(O,F) (456.88 and 462.88 eV), and C–Ti–F (458.64 and 464.64 eV), corresponding to the Ti $2p_{3/2}$ and Ti $2p_{1/2}$ orbitals (Fig. 1(e)) [44, 45]. For the Co 2p spectrum (Fig. 1(f)), the peaks at 781.42 and 791.07 eV correlate with Co^0 $2p_{3/2}$ and Co^0 $2p_{1/2}$, which illustrates the reduction of Co^{2+} to produce metallic Co particles. The two peaks at 783.94 and 799.73 eV correspond to Co^{2+}, indicating that Co nanoparticles are partially oxidized [46, 47]. In Fig. 1(g), the primary peaks at 874.77 and 857.62 eV are assigned to Ni $2p_{1/2}$ and Ni $2p_{3/2}$ orbitals, demonstrating the successful introduction of magnetic particles Ni [48]. These abundant functional groups can effectively promote dipole and defect polarization, improving the MA performance of EMW [22]. The XPS analytical results are consistent with those of the XRD demonstrating that the MMCNC composites were successfully prepared. The magnetic properties of the CNC and MMCNC were analyzed by VSM, as shown in Fig. 1(h). The saturation magnetization strengths of CNC and MMCNC were 36.11 and 11.05 emu/g, and the coercivities reached 224.17 and 293.22 Oe, respectively. MMCNC foam has weaker magnetic properties than CNC, which is owing to the presence of non-magnetic components (MF, MXene) [49, 50]. In addition, the MMCNC foam is firmly held without falling under the gravitational pull of the magnet (Fig. 1(i)).

The micromorphology of all samples was characterized by SEM images. The MF has a distinctive 3D porous network structure with extraordinarily high porosity, which facilitates MXene adsorption and deposition (Fig. S3(a) in the ESM). After immersing the MF into MXene solution, the MXene sheets can be firmly deposited on the backbones and pores of the MF (Figs. 2(a) and 2(b)). The adsorption of MXene sheets provided abundant sites for growth of Co and Ni ions. As shown in Figs. 2(c) and 2(d), the CNC particles with dimensions of ca. 500 nm were firmly adsorbed on the surface of the MM by electrostatic adsorption, which endowed the MM composites with strong magnetism. The microstructure of MMCNC was further shown in TEM and HRTEM images (Figs. 2(e)–2(h)). Figures 2(e) and 2(f) visually show the morphological characteristics of MMCNC, where CNC particles are uniformly deposited on MXene (Ti_3C_2) sheets. The HRTEM images demonstrate that the lattice spacings of 0.206 and 0.34 nm correspond to CoNi(111) crystal face and graphitized carbon(002) crystal face, respectively. The graphitized carbon layer tightly envelopes CoNi particles to form core–shell structure (Figs. 2(g) and 2(h)). The elemental mapping images in Figs. 2(i)–2(m) show that elements C, Ti, Co, and Ni are equally distributed, further proving the successful preparation of MF/MXene/CoNi@C composites.

3.2 EM properties

The EM absorption capabilities of the materials mainly depend on the effects of complex permittivity ($\varepsilon_r = \varepsilon' - j\varepsilon''$) and relative complex permeability ($\mu_r = \mu' - j\mu''$), where the real (ε' and μ') and imaginary (ε'' and μ'') parts represent the storage and decay

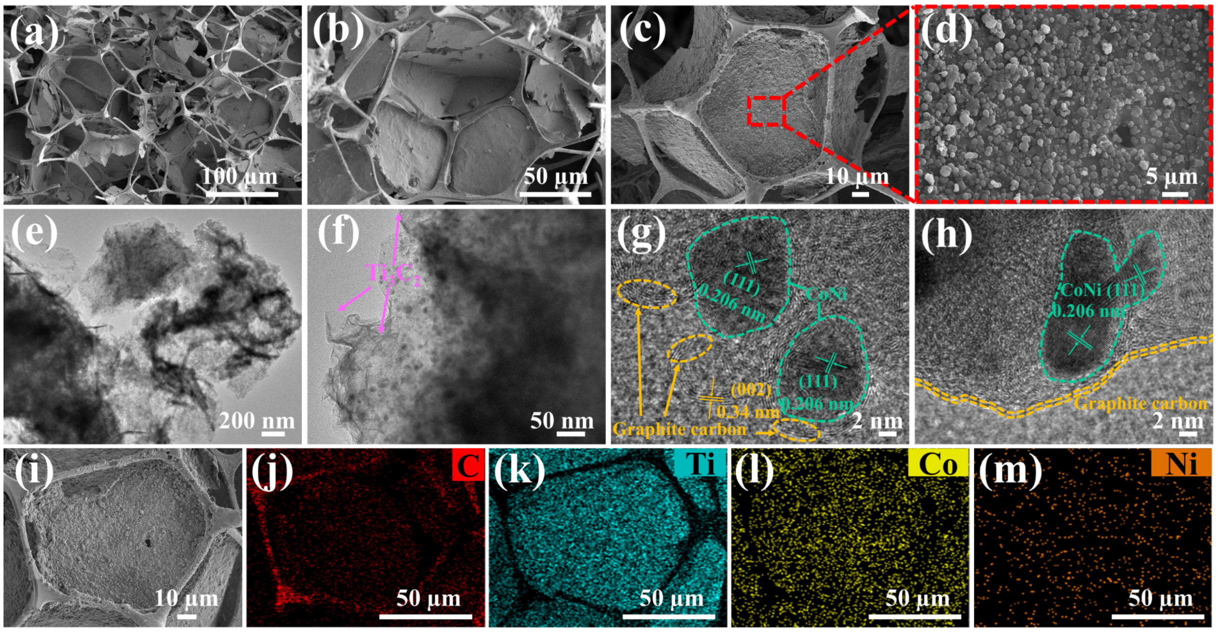

Figure 2 SEM images of (a) and (b) MM and (c) and (d) MMCNC. (e)–(h) TEM and HRTEM images of MMCNC. (i)–(m) Elemental mapping images of MMCNC.

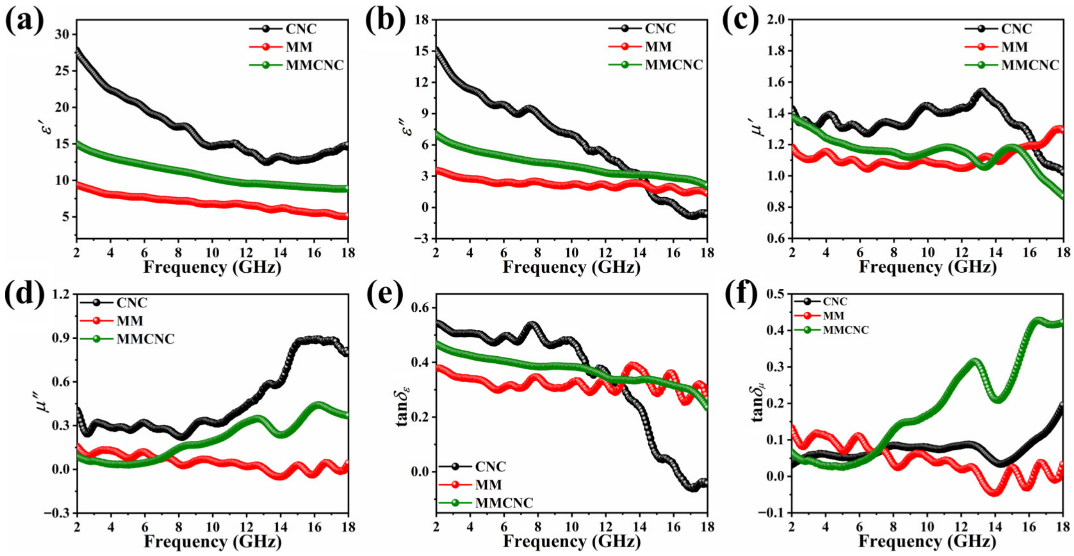

Figure 3 EM parameters of samples: (a) ε', (b) ε'', (c) μ', and (d) μ''. (e) Dielectric loss tangent and (f) magnetic loss tangent of samples.

capacities of the EMW, respectively [51–54]. The EM parameters of all samples in the 2–18 GHz range are shown in Fig. 3 and Fig. S4 in the ESM. The pure MF is inherently nonconducting and nonmagnetic, with low EM parameters, indicating poor attenuating ability (Figs. S4(a) and S4(b) in the ESM). The dielectric constants of CNC, MM, and MMCNC follow the same trend of dropping with increasing frequency over the whole frequency range. The values of ε' and ε'' for CNC decrease from 27.8 and 15.1 to 14.8 and 0.1. The values of ε' for MM and MMCNC decrease from 9.4 and 15.0 to 5.1 and 8.8, and the values of ε'' are in the range of between 3.6–1.3 and 7.0–2.1 (Figs. 3(a) and 3(b)). Among all the samples, CNC presents the highest ε' and ε'' values, which may be attributed to the presence of the highly conductive graphitized carbon layer after high-temperature calcination [46]. According to the free electron theory ($\varepsilon'' = 1/2\pi\varepsilon_0\sigma f$), the ε'' values rise with the conductivity [55, 56]. The ε' and ε'' values of both MM and MMCNC are greater than those of MF, suggesting that the introduction of highly conductive MXene sheets and CoNi particles increased the composites' complex permittivity level [57]. In addition, the fluctuation of peaks in the ε'' curves can be ascribed to the polarization relaxation processes, which come from the interfacial polarization, dipole polarization, and defect polarization [22]. Based on the Debye relaxation theory, Cole–Cole diagrams were drawn to further analyze the dielectric loss and relaxation process based on Eqs. (1)–(3) [58, 59]

$$\varepsilon' = \varepsilon_\infty + \frac{\varepsilon_s - \varepsilon_\infty}{1 + \omega^2\tau^2} \tag{1}$$

$$\varepsilon'' = \frac{\varepsilon_s - \varepsilon_\infty}{1 + \omega^2\tau^2}\omega\tau + \frac{\sigma}{\omega\varepsilon_0} \tag{2}$$

$$\left(\varepsilon' - \frac{\varepsilon_s + \varepsilon_\infty}{2}\right)^2 + (\varepsilon'')^2 = \left(\frac{\varepsilon_s - \varepsilon_\infty}{2}\right)^2 \tag{3}$$

where ε_s is the static permittivity at the high-frequency limit, ε_∞ is the relative permittivity, ω denotes the angular frequency, and τ and σ are the polarization relaxation and conductivity of the materials, respectively [29, 30]. Straight lines and semicircles on the Cole–Cole curves represent the conductive loss and polarization relaxation processes, respectively [60]. Figures S3(b)–S3(d) in the ESM show that all samples have straight lines and semicircles, demonstrating the coexistence of conductive and polarization relaxations. The incorporated MXene sheets perfectly combine with the 3D skeleton of the MF to form a distinctive 3D conductive transport network structure, thus increasing the conductive loss [22, 61]. The dielectric relaxation should mainly derive from dipole polarizations that was induced by the polar molecules and defects of the samples. On one hand, XPS results in Fig. 1 proved that MXene sheets possess abundant polar molecules and the rearrangement of intrinsic dipole under external EM field will induce the occurrence of orientation polarization. On the other hand, EPR results (Fig. S5 in the ESM) indicated that the MXene and CoNi@C surface possessed oxygen vacancies, which could trap charge carriers and break the balance of charge distribution, thus leading to polarization process under alternating EM field [62]. Besides, CoNi magnetic particles are electrostatically assembled on the MM surface, forming multiple heterogeneous interfaces causing interfacial polarization [63]. In addition, the accumulation and rearrangement of substantial space charges inside the MMCNC can also induce the interfacial polarization process and further enhance the dielectric loss.

The complex permeability of the materials is shown in Figs. 3(c) and 3(d), in which the magnetic CNC and MMCNC displayed larger levels than non-magnetic MM. The μ' and μ'' curves of CNC and MMCNC displayed multiple resonance peaks between 5–8 and 13–18 GHz, which can be attributed to the effects of natural resonance and exchange resonance, respectively, according to Toneguzzo et al.'s study [64]. The dielectric loss tangent ($\tan\delta_\varepsilon = \varepsilon''/\varepsilon'$) and magnetic loss tangent ($\tan\delta_\mu = \mu''/\mu'$) were utilized to evaluate the dielectric and magnetic losses of the materials (Figs. 3(e) and 3(f)) [65]. In Figs. 3(e) and 3(f), the trend of $\tan\delta_\varepsilon$ values for all the samples is comparable to the ε'' curve, confirming the effect of the multiple polarization relaxation process on the dielectric loss.

The MA capability of the samples is assessed by calculating the RL and EAB values according to the transmission line theory, and the equations are calculated as follows [66, 67]

$$Z_{\mathrm{in}} = Z_0(\mu_r/\varepsilon_r)^{1/2}\tanh\left\{\mathrm{j}(2\pi fd/c)(\mu_r\varepsilon_r)^{1/2}\right\} \quad (4)$$

$$\mathrm{RL}\,(\mathrm{dB}) = 20\log|(Z_{\mathrm{in}} - Z_0)/(Z_{\mathrm{in}} + Z_0)| \quad (5)$$

where Z_{in} represents the input impedance, Z_0 is the free space impedance, f is the EMW frequency, d denotes the thickness, and c is the speed of light [68]. It is generally considered that RL < −10 dB represents more than 90% of the EMW energy absorbed, and the corresponding frequency band is called the EAB [69]. The calculated RL, EAB, and impedance matching distributions for all samples are shown in Fig. 4 and Fig. S4 in the ESM. It is evident from Fig. S4(c) in the ESM that the MA of pure MF is very poor. The CNC has weak MA capability, with an RL of −17.76 dB (15.04 GHz) and an EAB of 4.64 GHz (13.36–18 GHz) at 1.02 mm (Figs. 4(a) and 4(d)). This is mostly due to the impedance mismatch caused by the high dielectric constant level. The MA capability of the MM samples after introducing MXene sheets is improved compared with pure MF, and the RL reaches up to −24.96 dB, with

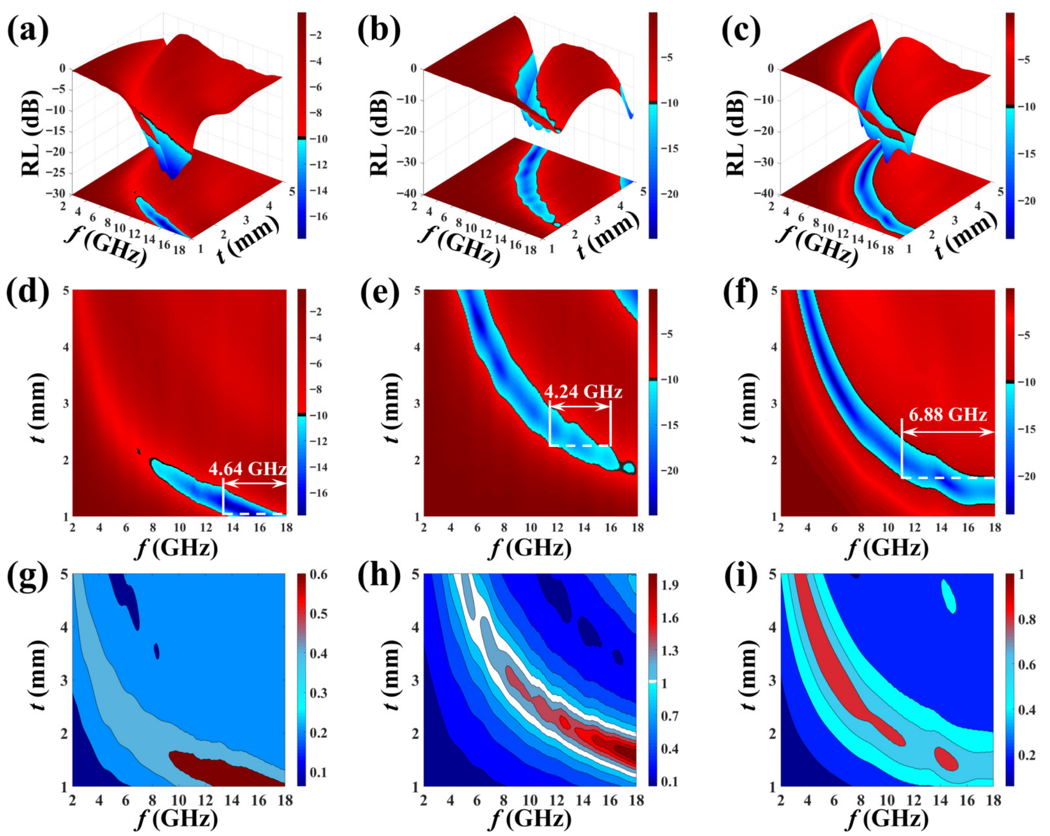

Figure 4 3D RL, 2D EAB, and impedance matching maps for (a), (d), and (g) CNC, (b), (e), and (h) MM, and (c), (f), and (i) MMCNC.

an EAB of 4.24 GHz (11.68–15.92 GHz) at 2.23 mm (Figs. 4(b) and 4(e)). In order to study the effect of MXene content on the EM properties, the EM parameters and MA performances of the MM composites under MXene concentrations of 2.0 and 10.0 mg/mL were evaluated, respectively. Figure S6 in the ESM showed that when the MXene concentration was equal to 2.0 mg/mL, the permittivity level of the MF@MXene composites was rather low due to the weak conductivity, which also led to a rather poor MA (Figs. S6(a) and S6(b) in the ESM). When the MXene concentration was improved to 10.0 mg/mL, the real and imaginary permittivity was largely enhanced. However, due to the overlarge EM parameters, the optimal RL was only −14.3 dB (Figs. S6(c) and S6(d) in the ESM). On the contrary, the permittivity of the samples with 5 mg/mL MXene was located at a proper level, which is also beneficial for the decoration of CoNi articles. Based on the discussions, the optimal MXene concentration of 5.0 mg/mL was selected for further modifications.

When CoNi magnetic particles were assembled with MM, MMCNC exhibited excellent MA capability. The optimal RL is −24.1 dB, and the EAB is widest up to 6.88 GHz (11.12–18 GHz), corresponding to a thickness of only 1.68 mm (Figs. 4(c) and 4(f)), totally encompassing the Ku band. The assembly of CoNi particles provides magnetic loss that modulates the EM parameters and enhances the absorption of EMW. Compared with sample MF and MM, the sample MMCNC displayed largely enhanced MA attributed to the synergistic effect of dielectric and magnetic losses, which optimized the impedance matching. The availability of good impedance matching and EMW attenuation properties determines the MA performance of the materials [70]. The closer of the $|Z_{in}/Z_0|$ value is to 1, the more perfect of the impedance matching is, suggesting that more EMW was absorbed than reflected [71]. Figure 4(g) showed that the area distribution of the $|Z_{in}/Z_0|$ values for CNC is lower than 1, which exhibits inferior impedance matching characteristics attributed to their high dielectric constant levels. Whereas, the regions with $|Z_{in}/Z_0|$ values close to 1 are larger for MM and MMCNC, which are favorable for more EMW to enter the materials and be absorbed (Figs. 4(h) and 4(i)). The incorporation of MXene sheets and subsequent assembly of CoNi magnetic particles produced a synergistic effect of dielectric/magnetic loss. This synergistic action can effectively regulate the dielectric constant level of the composites and optimize the impedance matching, thus exhibiting excellent MA capability.

To visually compare the MA performance of different samples, the optimal RL and EAB cylindrical distribution charts of the samples at various thicknesses are presented in Figs. 5(a) and 5(b). Compared with other samples, the optimal RL of MMCNC at different thicknesses is virtually always below −20 dB and shows the widest EAB of 6.88 GHz, which entirely covers the Ku band. Furthermore, the EAB levels at different bands can be adjusted by changing the thickness. For the MMCNC sample, the frequency range could cover 94% of the X band when the thickness was adjusted to 2.22 mm (Fig. 5(c)). The shift of the frequency range under different thickness can be explained by the quarter wavelength model ($t_m = \frac{n\lambda}{4} = \frac{nc}{4f_m\sqrt{|\varepsilon_r/\mu_r|}}(n = 1, 3, 5, \ldots)$), according to which the optimal RL moved towards the lower frequency region with the increasing thickness. Figure S7 in the ESM showed that the as-obtained MMCNC foams obeyed the quarter wavelength model and the frequency range with RL lower than −10 dB could be changed to other bands by adjusting the thickness [72, 73]. Figure 5(d) compared the MA performance of this research with previously reported MXene-based MAMs and found that the MMCNC composites have the advantages of wider EAB and thinner thickness, which can meet the demand of the development for the lightweight and broadband of modern electronic products [25, 51, 74–79].

The radar cross section (RCS) is used to characterize the stealth

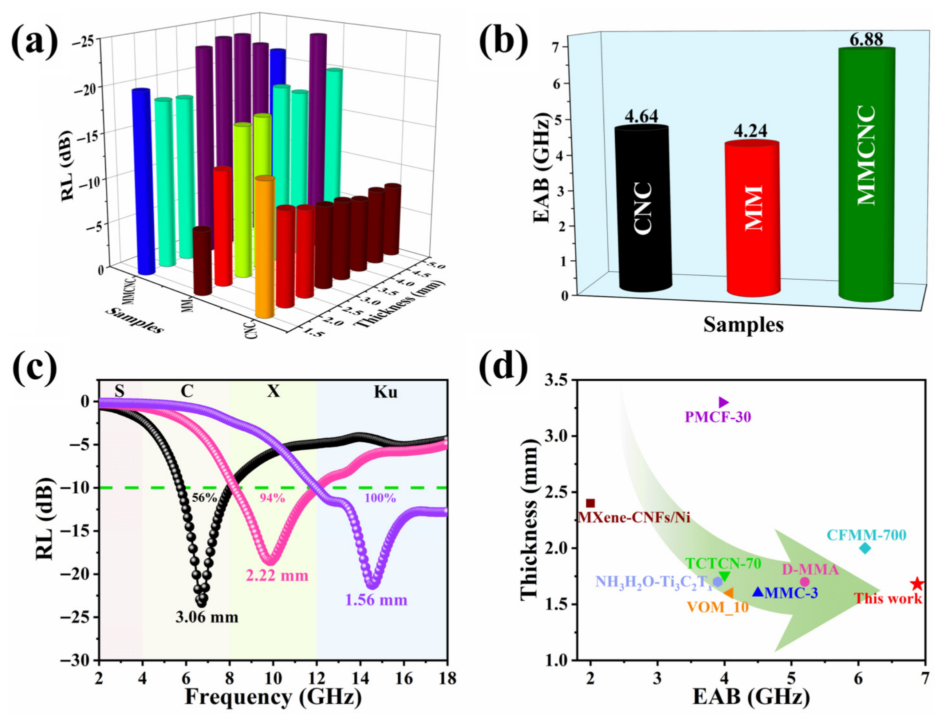

Figure 5 (a) RL cylindrical distribution of samples at different thicknesses. (b) EAB of samples. (c) RL and EAB of MMCNC. (d) Comparison between the recently reported MA of MXene-based MAMs and this research.

capability of a target under radar detection. It is generally assumed that the lower RCS values mean the better the stealth capability and the RCS values can be obtained by the following Eq. (6) [80–82]

$$\sigma\left(\mathrm{dBm}^2\right)=10\log\left(\frac{4\pi S}{\lambda^2}\left|\frac{E_\mathrm{S}}{E_\mathrm{i}}\right|\right)^2 \tag{6}$$

where S is the area of the target simulation model, λ is the wavelength of the EMW, and E_s and E_i represent the electric field strength of the scattered and incident waves, respectively. We provide the simulation model of the sample coated on a perfect electrical conductor (PEC) plate in Fig. 6. Compared to the original PEC plate, the RCS signal strength of the PEC plates coated with MF, CNC, and MM did not decrease significantly, while the RCS signal strength of the PEC plate with MMCNC strongly attenuated (Figs. 6(a)–6(e)). In addition, Fig. 6(f) reveals that only the MMCNC-coated PEC plates remain below −10 dBm^2 across practically the entire angular range, demonstrating that MMCNC has the best radar wave dissipation capabilities.

Based on the above analysis, the MA mechanism of the MMCNC composite is shown in Fig. 7. Firstly, the porous conductive network structure constructed inside the MMCNC promotes electron transition and enhances the conduction loss, thus attenuating the incident EMW. On the one hand, the formation of multiple heterogeneous interfaces between MXene sheets, CoNi magnetic particles, and MF backbone causes the aggregation of space charge and generates abundant interfacial polarization. On the other hand, the abundant functional groups and intrinsic defects on the surface of MMCNC can operate as polarization centers to induce dipole polarization. Meanwhile, the “micro-capacitor” structure formed by the assembly of MXene sheets and CoNi magnetic particles provides a place for charge accumulation and transmission, further enhancing the attenuation of EMW energy. Secondly, the distinctive 3D skeleton structure facilitates multiple reflections and scattering of the incident EMW, further enhancing the MMCNC attenuation characteristics. In addition, the CoNi magnetic particles provide magnetic loss, which attenuates the EMW energy via exchange and natural resonance. Overall, the synergistic effect of multiple loss mechanisms results in

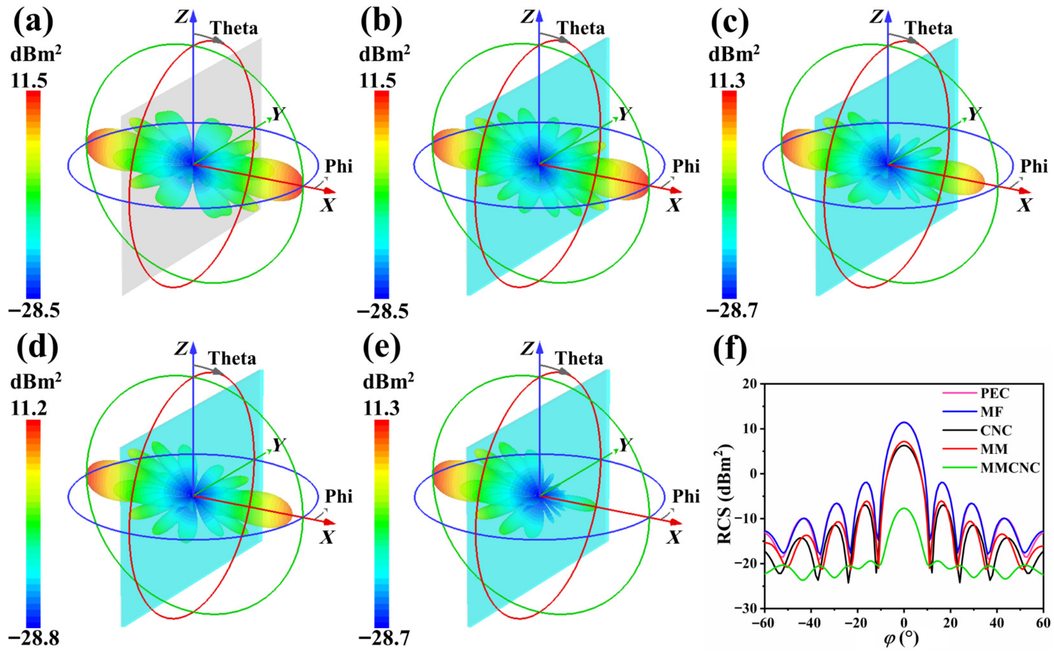

Figure 6 3D RCS radar reflection simulations diagrams of (a) PEC, (b) MF, (c) CNC, (d) MM, and (e) MMCNC. (f) RCS simulation curves of as-prepared samples.

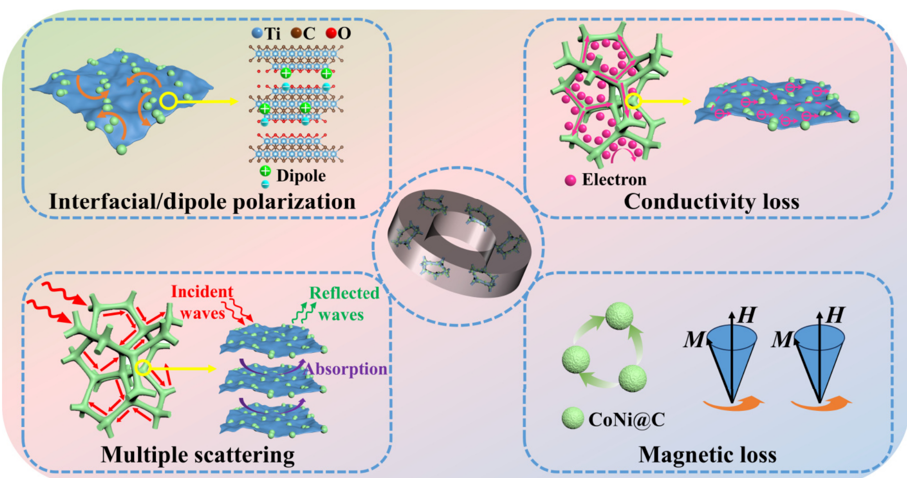

Figure 7 MA mechanism diagram of MMCNC.

the MMCNC composite with excellent MA capabilities.

3.3 Multifunctions

Due to the plasma resonance effect of MXene, the MMCNC composites have efficient photothermal conversion capabilities in addition to excellent MA performance [83]. Under the irradiation of a near-infrared laser (808 nm wavelength), the surface temperature of MMCNC rapidly rises to the maximum equilibrium temperature, and the temperature increases with the increase of optical power density. The surface equilibrium temperature rose from 39.9 to 106.9 °C as the power density increased from 25 to 200 mW/cm^2 (Fig. 8(a)). When the laser is switched off, the surface temperature rapidly cools to ambient temperature, showing fully reversible photothermal conversion performance. In addition, real-time control of the composite surface temperature can be realized by adjusting the optical power density (Fig. 8(b)). This photothermal process is recorded by the infrared thermogram of Fig. 8(c), and the surface temperature of MMCNC is evenly distributed, showing excellent photothermal stability and reliability.

As an excellent MA material, it should have outstanding infrared stealth performance, preventing electronic equipment or military weapons from being attacked by infrared detectors [13, 84]. The MMCNC was put on a heating platform at 100 °C, and infrared thermal imaging was acquired every 5 min (5 s–10 min) as shown in Fig. 9(a). The detected temperatures of the samples were 47.3, 52.8, and 53.3 °C, which were much lower than the heating platform. Moreover, the temperature of the MMCNC remained almost constant during the heating process, showing that it has excellent thermal isolation stability. Figure 9(b) demonstrates the smooth temperature change trend of MMCNC with time changes, which systematically exhibits that MMCNC has outstanding thermal insulation performance. In addition, the superior thermal insulation performance is the key to ensuring that MMCNC has infrared stealth performance. Figure 9(c) depicts the thermal image of MMCNC placed on the hand, with the sample temperature of only 29.2 °C, which is much lower than that of the temperature of the human body (38 °C). It demonstrates that the area covered by the sample can have a significant stealth effect under the infrared detection device.

The excellent infrared stealth performance of MMCNC is closely related to its material and distinctive structure. Firstly, MXene is considered an excellent candidate for thermal insulation and IR

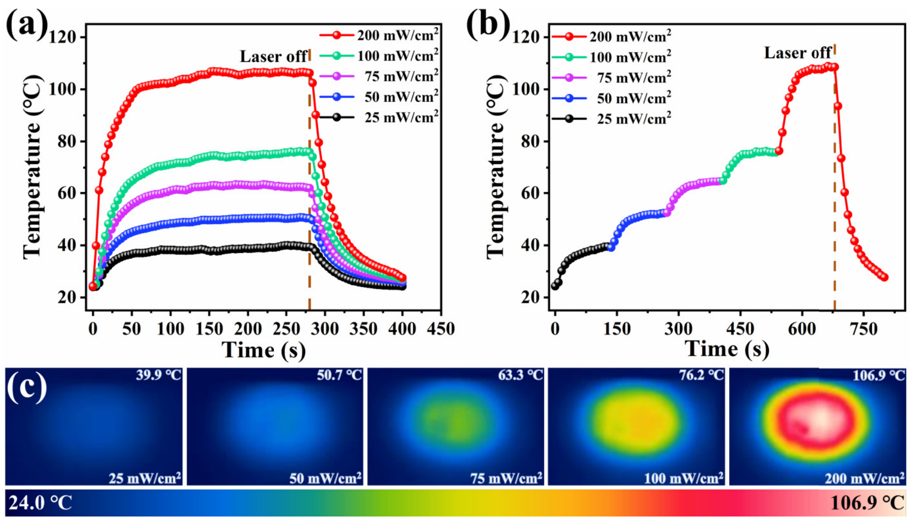

Figure 8 (a) and (b) Photothermal profiles of MMCNC at different optical power densities and progressively increasing optical power densities. (c) Thermal infrared images of MMCNC.

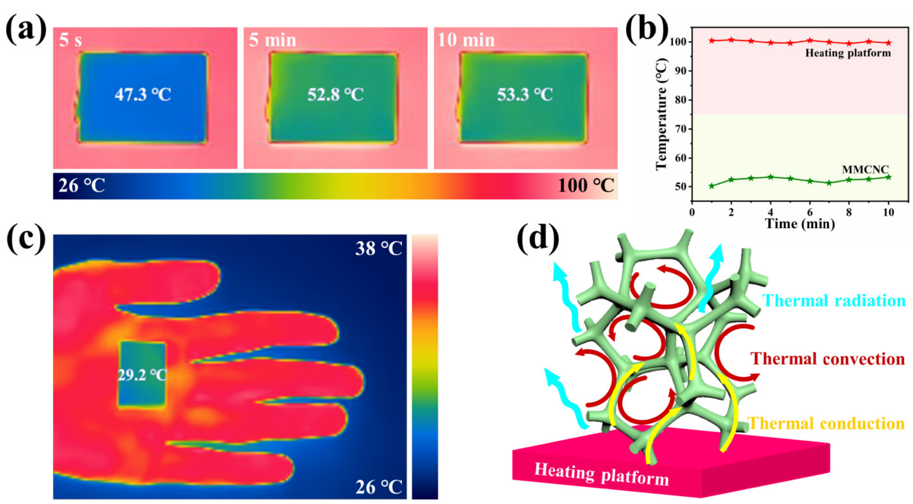

Figure 9 (a) and (b) Thermal infrared images and temperature change curves of MMCNC at different heating times on the heating platform. (c) Thermal infrared image of MMCNC in hand. (d) Heat transfer mechanism diagram of MMCNC.

stealth owing to its quite low infrared emissivity, which could significantly decrease the radiative heat and lower the possibility of being captured by the infrared detecting device [85, 86]. Secondly, the heat transfer modes are classified as thermal conduction, thermal convection, and thermal radiation, which depend on solid-phase heat transfer, vapor-phase heat transfer, and radiative heat transfer, respectively (Fig. 9(d)) [35, 87]. MF has the advantages of a 3D porous skeleton structure with a low density and high porosity, significantly reducing the intensity of solid-phase and radiative heat transfer. Furthermore, the long skeleton of MF can extend the heat transfer path and thus attenuate the heat transfer intensity. Therefore, MMCNC has exceptional infrared stealth performance, which displayed broad potential for application in military camouflage and stealth technologies.

4 Conclusions

In summary, the multifunctional MMCNC foams composed of 3D melamine skeleton, few-layer MXene sheets, and MOFs derived CoNi@C nanoparticles were successfully prepared via vacuum impregnation and electrostatic self-assembly processes. The multi-component design and distinctive 3D porous structure provide the foam with perfect impedance matching and strong attenuation capability. The synergistic effects of dipole/interfacial polarization, dielectric/magnetic losses, and multiple scattering significantly improve the MA performance of the samples. The ultimate MMCNC samples have an RL value of –24.1 dB and an EAB as high as 6.88 GHz, corresponding to a thickness of only 1.68 mm and completely covering the Ku band. In addition, the MMCNC composite foams have excellent photothermal conversion, thermal insulation, and infrared stealth capabilities, which can ensure the normal operation of electronic devices in extreme environments. Therefore, this study opens new prospects for developing multifunctional MAMs for practical applications.

Electronic Supplementary Material: Supplementary material (XRD, SEM, TEM images, zeta potential, XPS, Cole–Cole semicircles, EPR and FITR spectrum, EM parameters, and video) is available in the online version of this article at https://doi.org/10.26599/NR.2025.94907121.

Data availability

All data needed to support the conclusions in the paper arepresented in the manuscript and the Electronic Supplementary Material. Additional data related to this paper may be requested from the corresponding author upon request.

Acknowledgements

The authors acknowledge the support from Natural Science Foundation of Shandong Province (No. ZR2021QE164) and research fund of Shandong University of Science and Technology. The author would like to thank Yali Zhang from Shiyanjia Lab (www.shiyanjia.com) for the XPS analysis.

Declaration of competing interest

All the contributing authors report no conflict of interests in this work.

Author contribution statement

N. N. W.: Data curation, project administration, validation, writing manuscript, experimental design. Z. Y. S.: Data curation, project administration, validation, experimental design, writing manuscript. Y. T. M.: Project administration, validation. Z. Z. W.: Validation, experimental design. C. X. H.: Project administration, funding acquisition. S. J. G.: Project administration, funding acquisition. J. T.: Project administration, funding acquisition. J. R. L.: Project administration, funding acquisition. All the authors have approved the final manuscript.

Use of AI statement

None.

References

[1] Hao, Z. W.; Zhou, J.; Lin, S. N.; Lan, D.; Li, H. Y.; Wang, H.; Liu, D.; Gu, J. W.; Wang, X. B.; Wu, G. L. Customized heterostructure of transition metal carbides as high-efficiency and anti-corrosion electromagnetic absorbers. *Carbon* **2024**, *228*, 119323.

[2] Hu, K. X.; Wang, H. H.; Zhang, X.; Huang, H.; Qiu, T.; Wang, Y.; Zhang, C. F.; Pan, L. M.; Yang, J. Ultralight $Ti_3C_2T_x$ MXene foam with superior microwave absorption performance. *Chem. Eng. J.* **2021**, *408*, 127283.

[3] Zhang, Z. W.; Cai, Z. H.; Zhang, Y.; Peng, Y. L.; Wang, Z. Y.; Xia, L.; Ma, S. P.; Yin, Z. Z.; Wang, R. F.; Cao, Y. S. et al. The recent progress of MXene-based microwave absorption materials. *Carbon* **2021**, *174*, 484–499.

[4] Jia, Z. R.; Liu, J. K.; Gao, Z. G.; Zhang, C. H.; Wu, G. L. Molecular intercalation-induced two-phase evolution engineering of 1T and 2H-MS_2 (M = Mo, V, W) for interface-polarization-enhanced electromagnetic absorbers. *Adv. Funct. Mater.*, in press, https://doi.org/10.1002/adfm.202405523.

[5] Zhang, Y.; Zuo, X. P.; Zhang, S.; Ma, Z. L.; Zhang, G. C. Flexible multifunctional magnetic-conductive Janus nanocomposite films towards highly-efficient electromagnetic interference shielding and thermal management. *Compos. Sci. Technol.* **2024**, *256*, 110756.

[6] Zhang, Y.; Wang, J.; Wu, Q. L.; Shan, T.; Bai, S. J.; Lan, D.; Zhang, B.; Liu, Y. Q.; Su, X. G. Enhanced electromagnetic wave absorption of bacterial cellulose/ reduced graphene oxide aerogel by eco-friendly *in-situ* construction. *J. Colloid Interface Sci.* **2025**, *678*, 648–655.

[7] Cui, Y. H.; Wu, F.; Wang, J. Q.; Wang, Y. B.; Shah, T.; Liu, P.; Zhang, Q. Y.; Zhang, B. L. Three dimensional porous MXene/CNTs microspheres: Preparation, characterization and microwave absorbing properties. *Compos. Part A: Appl. Sci. Manuf.* **2021**, *145*, 106378.

[8] Cheng, J. Y.; Zhang, H. B.; Wang, H. H.; Huang, Z. H.; Raza, H.; Hou, C. X.; Zheng, G. P.; Zhang, D. Q.; Zheng, Q. B.; Che, R. C. Tailoring self-polarization of bimetallic organic frameworks with multiple polar units toward high-performance consecutive multi-band electromagnetic wave absorption at gigahertz. *Adv. Funct. Mater.* **2022**, *32*, 2201129.

[9] Zhu, J. H.; Lan, D.; Liu, X. H.; Zhang, S. H.; Jia, Z. R.; Wu, G. L. Porous structure fibers based on multi-element heterogeneous components for optimized electromagnetic wave absorption and self-anticorrosion performance. *Small*, in press, https://doi.org/10.1002/smll.202403689.

[10] Zhou, Z. H.; Lan, D.; Ren, J. W.; Cheng, Y. H.; Jia, Z. R.; Wu, G. L.; Yin, P. F. Controllable heterogeneous interfaces and dielectric modulation of biomass-derived nanosheet metal-sulfide complexes for high-performance electromagnetic wave absorption. *J. Mater. Sci. Technol.* **2024**, *185*, 165–173.

[11] Xie, X. B.; Wang, H. S.; Kimura, H.; Ni, C.; Du, W.; Wu, G. L. NiCoZn/C@melamine sponge-derived carbon composites with high-

performance electromagnetic wave absorption. *Int. J. Miner. Metall. Mater.* **2024**, *31*, 2274–2286.

[12] Cao, M. S.; Cai, Y. Z.; He, P.; Shu, J. C.; Cao, W. Q.; Yuan, J. 2D MXenes: Electromagnetic property for microwave absorption and electromagnetic interference shielding. *Chem. Eng. J.* **2019**, *359*, 1265–1302.

[13] Cheng, H. R.; Pan, Y. M.; Wang, X.; Liu, C. T.; Shen, C. Y.; Schubert, D. W.; Guo, Z. H.; Liu, X. H. Ni Flower/MXene-melamine foam derived 3D magnetic/conductive networks for ultra-efficient microwave absorption and infrared stealth. *Nano-Micro Lett.* **2022**, *14*, 63.

[14] Zhang, S. J.; Zheng, J. J.; Lan, D.; Gao, Z. G.; Liang, X. W.; Tian, Q. F.; Zhao, Z. W.; Wu, G. L. Hierarchical engineering on built-in electric field of bimetallic zeolitic imidazolate derivatives towards amplified dielectric loss. *Adv. Funct. Mater.*, in press, https://doi.org/10.1002/adfm.202413884.

[15] Jia, Z. R.; Sun, L. F.; Gao, Z. G.; Lan, D. Modulating magnetic interface layer on porous carbon heterostructures for efficient microwave absorption. *Nano Res.* **2024**, *17*, 10099–10108.

[16] Shen, X.; Kim, J. K. Graphene and MXene-based porous structures for multifunctional electromagnetic interference shielding. *Nano Res.* **2023**, *16*, 1387–1413.

[17] He, Y. F.; Su, Q.; Liu, D. D.; Xia, L.; Huang, X. X.; Lan, D.; Liu, Y. N.; Huang, Y. D.; Zhong, B. Surface engineering strategy for MXene to tailor electromagnetic wave absorption performance. *Chem. Eng. J.* **2024**, *491*, 152041.

[18] Su, X. G.; Zhang, Y.; Wang, J.; Liu, Y. Q. Enhanced electromagnetic wave absorption and mechanical performances of graphite nanosheet/PVDF foams via ice dissolution and normal pressure drying. *J. Mater. Chem. C* **2024**, *12*, 7775–7783.

[19] Tang, X. W.; Zhao, X.; Lu, Y. Z.; Li, S. S.; Zhang, Z. H.; Zhu, M. Y.; Yao, K. Q.; Zheng, J. X.; Chen, H. J.; Duan, Y. Q. et al. Flexible metalized polyimide nonwoven fabrics for efficient electromagnetic interference shielding. *Chem. Eng. J.* **2024**, *480*, 148000.

[20] Cheng, J.; Cai, L.; Shi, Y. Y.; Pan, F.; Dong, Y. Y.; Zhu, X. J.; Jiang, H. J.; Zhang, X.; Xiang, Z.; Lu, W. Polarization loss-enhanced honeycomb-like MoS_2 nanoflowers/undaria pinnatifida-derived porous carbon composites with high-efficient electromagnetic wave absorption. *Chem. Eng. J.* **2022**, *431*, 134284.

[21] Han, Y.; Lan, D.; Han, M. J.; Xia, Z. H.; Zou, J. X.; Jia, Z. R. Construction of flower-like MoS_2 decorated on Cu doped CoZn-ZIF derived N-doped carbon as superior microwave absorber. *Nano Res.* **2024**, *17*, 8250–8260.

[22] Li, S. S.; Mo, W. J.; Liu, Y.; Wang, Q. Constructing 3D tent-like frameworks in melamine hybrid foam for superior microwave absorption and thermal insulation. *Chem. Eng. J.* **2023**, *454*, 140133.

[23] Song, Q.; Ye, F.; Kong, L.; Shen, Q. L.; Han, L. Y.; Feng, L.; Yu, G. J.; Pan, Y. A.; Li, H. J. Graphene and MXene nanomaterials: Toward high-performance electromagnetic wave absorption in gigahertz band range. *Adv. Funct. Mater.* **2020**, *30*, 2000475.

[24] Xu, B.; Gogotsi, Y. MXenes: From discovery to applications. *Adv. Funct. Mater.* **2020**, *30*, 2007011.

[25] Liu, Z. K.; Chen, J.; Que, M. D.; Zheng, H. Q.; Yang, L. F.; Yuan, H. D.; Ma, Y. Z.; Li, Y. J.; Yang, X. F. 2D $Ti_3C_2T_x$ MXene/MOFs composites derived CoNi bimetallic nanoparticles for enhanced microwave absorption. *Chem. Eng. J.* **2022**, *450*, 138442.

[26] Cheng, H. R.; Pan, Y. M.; Li, W.; Liu, C. T.; Shen, C. Y.; Liu, X. H.; Pan, C. F. Facile design of multifunctional melamine foam with Ni-anchored reduced graphene oxide/MXene as highly efficient microwave absorber. *Nano Today* **2023**, *52*, 101958.

[27] Pan, F.; Yu, L. Z.; Xiang, Z.; Liu, Z. C.; Deng, B. W.; Cui, E. B.; Shi, Z.; Li, X.; Lu, W. Improved synergistic effect for achieving ultrathin microwave absorber of 1D Co nanochains/2D carbide MXene nanocomposite. *Carbon* **2021**, *172*, 506–515.

[28] Li, X.; You, W. B.; Wang, L.; Liu, J. W.; Wu, Z. C.; Pei, K.; Li, Y. S.; Che, R. C. Self-assembly-magnetized MXene avoid dual-agglomeration with enhanced interfaces for strong microwave absorption through a tunable electromagnetic property. *ACS Appl. Mater. Interfaces* **2019**, *11*, 44536–44544.

[29] Ning, Y. H.; Yang, M. L.; Zhao, Z. B.; Sun, X. X.; Yang, S.; Wang, S. S.; Liang, L.; Cheng, Y. J.; Yin, W. L.; Yuan, Y. et al. Anisotropic electromagnetic absorption of the aligned $Ti_3C_2T_x$ MXene/RGO nanocomposite foam. *Compos. Sci. Technol.* **2022**, *227*, 109609.

[30] Jia, Z. R.; Lan, D.; Chang, M.; Han, Y.; Wu, G. L. Heterogeneous interfaces and 3D foam structures synergize to build superior electromagnetic wave absorbers. *Mater. Today Phys.* **2023**, *37*, 101215.

[31] Zhang, Y.; Zhang, G. C.; Ma, Z. L.; Qin, J. B.; Shen, X. Heterogeneous MXene-based films with graded electrical conductivity towards highly efficient EMI shielding and electrothermal heating. *Nano Res.* **2024**, *17*, 7264–7274.

[32] Pan, F.; Cai, L.; Shi, Y. Y.; Dong, Y. Y.; Zhu, X. J.; Cheng, J.; Jiang, H. J.; Wang, X.; Jiang, Y. F.; Lu, W. Heterointerface engineering of β-chitin/carbon nano-onions/Ni-P composites with boosted Maxwell-Wagner-Sillars effect for highly efficient electromagnetic wave response and thermal management. *Nano-Micro Lett.* **2022**, *14*, 85.

[33] Zhang, Z. H.; Li, S. S.; Zhao, X.; Tang, X. W.; Lu, Y. Z.; Zhu, M. Y.; Chen, H. J.; Wang, Z. X.; Hu, Z. Y.; Long, L. J. et al. Lightweight polymethacrylimide based composites foam with efficient infrared stealth and microwave transparent performance. *Compos. Commun.* **2024**, *47*, 101865.

[34] Gao, Z. H.; Shi, Y. N.; Ma, L. X.; Du, J.; Qiu, J. Bioinspired hierarchical composite for multiband defense. *ACS Appl. Mater. Interfaces* **2024**, *16*, 49687–49700.

[35] Xu, Z. J.; Ding, X.; Li, S. K.; Huang, F. Z.; Wang, B. J.; Wang, S. P.; Zhang, X.; Liu, F. H.; Zhang, H. Oxidation-resistant MXene-based melamine foam with ultralow-percolation thresholds for electromagnetic-infrared compatible shielding. *ACS Appl. Mater. Interfaces* **2022**, *14*, 40396–40407.

[36] Shi, H. G.; Zhao, H. B.; Liu, B. W.; Wang, Y. Z. Multifunctional flame-retardant melamine-based hybrid foam for infrared stealth, thermal insulation, and electromagnetic interference shielding. *ACS Appl. Mater. Interfaces* **2021**, *13*, 26505–26514.

[37] Zhao, T. B.; Lan, D.; Jia, Z. R.; Gao, Z. G.; Wu, G. L. Hierarchical porous molybdenum carbide synergic morphological engineering towards broad multi-band tunable microwave absorption. *Nano Res.* **2024**, *17*, 9845–9856.

[38] Zhang, H.; Ma, H. Y.; Ma, Y. H.; Lou, Y. M.; Jiao, Y. H.; Xu, J. Z. Hierarchical boric acid/melamine aerogel based on reversible hydrogen bonds with robust fire resistance, thermal insulation and recycling properties. *Compos. Part B: Eng.* **2023**, *252*, 110507.

[39] Shi, H. D.; Yue, M.; Zhang, C. J.; Dong, Y. F.; Lu, P. F.; Zheng, S. H.; Huang, H. J.; Chen, J.; Wen, P. C.; Xu, Z. C. et al. 3D flexible, conductive, and recyclable $Ti_3C_2T_x$ MXene-melamine foam for high-areal-capacity and long-lifetime alkali-metal anode. *ACS Nano* **2020**, *14*, 8678–8688.

[40] Fan, L.; Zhuang, H. L.; Zhang, W. D.; Fu, Y.; Liao, Z. H.; Lu, Y. Y. Stable lithium electrodeposition at ultra-high current densities enabled by 3D PMF/Li composite anode. *Adv. Energy Mater.* **2018**, *8*, 1703360.

[41] Wu, D.; Lan, D.; Li, Y. Q.; Zhou, N. F.; He, Q. C.; Wang, Y. Q. Heterostructure engineering of N-doped Co@carbon nanotubes toward broadband efficient electromagnetic absorption. *Colloids Surf. A: Physicochem. Eng. Aspects* **2024**, *702*, 135161.

[42] Adomaviciute-Grabusove, S.; Popov, A.; Ramanavicius, S.; Sablinskas, V.; Shevchuk, K.; Gogotsi, O.; Baginskiy, I.; Gogotsi, Y.; Ramanavicius, A. Monitoring $Ti_3C_2T_x$ MXene degradation pathways using Raman spectroscopy. *ACS Nano* **2024**, *18*, 13184–13195.

[43] Su, X. G.; Wang, J.; Liu, T.; Zhang, Y.; Liu, Y. N.; Zhang, B.; Liu, Y. Q.; Wu, H. J.; Xu, H. X. Controllable atomic migration in microstructures and defects for electromagnetic wave absorption enhancement. *Adv. Funct. Mater.* **2024**, *34*, 2403397.

[44] Lu, Y. F.; Li, D. S.; Liu, F. Characterizing the chemical structure of $Ti_3C_2T_x$ MXene by angle-resolved XPS combined with argon ion etching. *Materials* **2022**, *15*, 307.
[45] Ma, W. J.; Cai, W. R.; Chen, W. H.; Liu, P. J.; Wang, J. F.; Liu, Z. X. A novel structural design of shielding capsule to prepare high-performance and self-healing MXene-based sponge for ultra-efficient electromagnetic interference shielding. *Chem. Eng. J.* **2021**, *426*, 130729.
[46] Liu, G. L.; Liu, X. F.; Song, Z. M.; Sun, X.; Li, Y.; Shui, J. L.; Yu, R. H. Hollow double-shell structured Void@SiO_2@Co-C composite for broadband electromagnetic wave absorption. *Chem. Eng. J.* **2021**, *417*, 128093.
[47] Shen, Z. Y.; Lan, D.; Cong, Y.; Lian, Y. Y.; Wu, N. N.; Jia, Z. R. Tailored heterogeneous interface based on porous hollow In-Co-C nanorods to construct adjustable multi-band microwave absorber. *J. Mater. Sci. Technol.* **2024**, *181*, 128–137.
[48] Liu, Y.; Ren, X. Y.; Zhou, X. F.; Lan, D.; Gao, Z. G.; Jia, Z. R.; Wu, G. L. Defect design and vacancy engineering of $NiCo_2Se_4$ spinel composite for excellent electromagnetic wave absorption. *Ceram. Int.* **2024**, *50*, 46643–46652.
[49] Xu, D. M.; Qiao, J.; Wu, N. N.; Liu, W.; Wang, F. L.; Lv, L. F.; Pan, J. B.; Dong, Y. Z.; Liu, J. R. Facile synthesis of three-dimensional porous Co/MnO composites derived from bimetal oxides for highly efficient electromagnetic wave absorption. *ACS Sustain. Chem. Eng.* **2019**, *7*, 8687–8695.
[50] Yang, N.; Luo, Z. X.; Zhu, G. R.; Chen, S. C.; Wang, X. L.; Wu, G.; Wang, Y. Z. Ultralight three-dimensional hierarchical cobalt nanocrystals/N-doped CNTs/carbon sponge composites with a hollow skeleton toward superior microwave absorption. *ACS Appl. Mater. Interfaces* **2019**, *11*, 35987–35998.
[51] Li, X.; You, W. B.; Xu, C. Y.; Wang, L.; Yang, L. T.; Li, Y. S.; Che, R. C. 3D seed-germination-like MXene with *in situ* growing CNTs/Ni heterojunction for enhanced microwave absorption via polarization and magnetization. *Nano-Micro Lett.* **2021**, *13*, 157.
[52] Zhang, S. J.; Lan, D.; Zheng, J. J.; Zhao, Z. W.; Jia, Z. R.; Wu, G. L. Insights into polarization relaxation of electromagnetic wave absorption. *Cell Rep. Phys. Sci.* **2024**, *5*, 102206.
[53] Dong, Y. H.; Lan, D.; Xu, S.; Gu, J. W.; Jia, Z. R.; Wu, G. L. Controllable fiberization engineering of cobalt anchored mesoporous hollow carbon spheres for positive feedback to electromagnetic wave absorption. *Carbon* **2024**, *228*, 119339.
[54] Tan, D. L.; Wang, Q.; Li, M. R.; Song, L. M.; Zhang, F.; Min, Z. Y.; Wang, H. L.; Zhu, Y. Q.; Zhang, R.; Lan, D. et al. Magnetic media synergistic carbon fiber@Ni/NiO composites for high-efficiency electromagnetic wave absorption. *Chem. Eng. J.* **2024**, *492*, 152245.
[55] Liu, D. W.; Yang, L.; Wang, F. Y.; Zhang, H.; Liu, J.; Lv, T.; Zhao, H. J.; Du, Y. C. Hierarchical carbon nanotubes@Ni/C foams for high-performance microwave absorption. *Carbon* **2022**, *196*, 867–876.
[56] Zhang, R. X.; Wang, L.; Xu, C. Y.; Liang, C. Y.; Liu, X. H.; Zhang, X. F.; Che, R. C. Vortex tuning magnetization configurations in porous Fe_3O_4 nanotube with wide microwave absorption frequency. *Nano Res.* **2022**, *15*, 6743–6750.
[57] Li, X.; Wu, Z. C.; You, W. B.; Yang, L. T.; Che, R. C. Self-assembly MXene-rGO/CoNi film with massive continuous heterointerfaces and enhanced magnetic coupling for superior microwave absorber. *Nano-Micro Lett.* **2022**, *14*, 73.
[58] Guo, Z. Q.; Lan, D.; Jia, Z. R.; Gao, Z. G.; Shi, X. T.; He, M. K.; Guo, H.; Wu, G. L.; Yin, P. F. Multiple tin compounds modified carbon fibers to construct heterogeneous interfaces for corrosion prevention and electromagnetic wave absorption. *Nano-Micro Lett.* **2025**, *17*, 23.
[59] Han, M. J.; Lan, D.; Zhang, Z. M.; Zhao, Y. Z.; Zou, J. X.; Gao, Z. G.; Wu, G. L.; Jia, Z. R. Micro-sized hexapod-like CuS/Cu_9S_5 hybrid with broadband electromagnetic wave absorption. *J. Mater. Sci. Technol.* **2025**, *214*, 302–312.
[60] Xu, X. Q.; Ran, F. T.; Lai, H.; Cheng, Z. J.; Lv, T.; Shao, L.; Liu, Y. Y. *In situ* confined bimetallic metal-organic framework derived nanostructure within 3D interconnected bamboo-like carbon nanotube networks for boosting electromagnetic wave absorbing performances. *ACS Appl. Mater. Interfaces* **2019**, *11*, 35999–36009.
[61] Yang, K.; Cui, Y. H.; Wan, L. Y.; Wang, Y. B.; Tariq, M. R.; Liu, P.; Zhang, Q. Y.; Zhang, B. L. Preparation of three-dimensional Mo_2C/NC@MXene and its efficient electromagnetic absorption properties. *ACS Appl. Mater. Interfaces* **2022**, *14*, 7109–7120.
[62] Qin, M.; Zhang, L. M.; Wu, H. J. Dielectric loss mechanism in electromagnetic wave absorbing materials. *Adv. Sci.* **2022**, *9*, 2105553.
[63] Jia, Z. R.; Zhang, X. Y.; Gu, Z.; Wu, G. L. MOF-derived Ni-Co bimetal/porous carbon composites as electromagnetic wave absorber. *Adv. Compos. Hybrid Mater.* **2023**, *6*, 28.
[64] Toneguzzo, P.; Viau, G.; Acher, O.; Fiévet-Vincent, F.; Fiévet, F. Monodisperse ferromagnetic particles for microwave applications. *Adv. Mater.* **1998**, *10*, 1032–1035.
[65] Cai, L.; Pan, F.; Zhu, X. J.; Dong, Y. Y.; Shi, Y. Y.; Xiang, Z.; Cheng, J.; Jiang, H. J.; Shi, Z.; Lu, W. Etching engineering and electrostatic self-assembly of N-doped MXene/hollow Co-ZIF hybrids for high-performance microwave absorbers. *Chem. Eng. J.* **2022**, *434*, 133865.
[66] Wu, N. N.; Zhao, B. B.; Lian, Y. Y.; Liu, S. S.; Xian, Y.; Gu, J. W.; Wu, G. L. Metal organic frameworks derived Ni_xSe_y@NC hollow microspheres with modifiable composition and broadband microwave attenuation. *Carbon* **2024**, *226*, 119215.
[67] Sun, C. H.; Lan, D.; Jia, Z. R.; Gao, Z. G.; Wu, G. L. Kirkendall effect-induced ternary heterointerfaces engineering for high polarization loss MOF-LDH-MXene absorbers. *Small*, in press, https://doi.org/10.1002/smll.202405874.
[68] Yang, X.; Xuan, L. X.; Men, W. W.; Wu, X.; Lan, D.; Shi, Y. P.; Jia, H. X.; Duan, Y. P. Carbonyl iron/glass fiber cloth composites: Achieving multi-spectrum stealth in a wide temperature range. *Chem. Eng. J.* **2024**, *491*, 151862.
[69] Yin, P. F.; Luo, Y. M.; Lan, D.; Wang, J.; Feng, X.; Jia, Z. R.; Wu, G. L.; Zhang, Y. Structural engineering of porous biochar loaded with ferromagnetic/anti-ferromagnetic $NiCo_2O_4$/CoO for excellent electromagnetic dissipation with flexible and self-cleaning properties. *J. Mater. Sci. Technol.* **2024**, *180*, 12–22.
[70] Zhang, H.; Zhao, Y. P.; Zuo, X. Q.; Huang, H.; Sun, C.; Fan, Z.; Pan, L. J. Construction of chiral-magnetic-dielectric trinity composites for efficient microwave absorption with low filling ratio and thin thickness. *Chem. Eng. J.* **2023**, *467*, 143414.
[71] Chang, Q. L.; Li, C. P.; Sui, J.; Waterhouse, G. I. N.; Zhang, Z. M.; Yu, L. M. Cage-like eggshell membrane-derived Co-Co_xS_y-Ni/N,S-codoped carbon composites for electromagnetic wave absorption. *Chem. Eng. J.* **2022**, *430*, 132650.
[72] Zhang, Y.; Lan, D.; Hou, T. Q.; Jia, M. S.; Jia, Z. R.; Gu, J. W.; Wu, G. L. Multifunctional electromagnetic wave absorbing carbon fiber/$Ti_3C_2T_X$ MXene fabric with ultra-wide absorption band. *Carbon* **2024**, *230*, 119594.
[73] Ma, G. J.; Lan, D.; Zhang, Y.; Sun, X. Y.; Jia, Z. R.; Wu, G. L.; Bu, G. X.; Yin, P. F. Microporous cobalt ferrite with bio-carbon loosely decorated to construct multi-functional composite for dye adsorption, anti-bacteria and electromagnetic protection. *Small* **2024**, *45*, 2404449.
[74] Du, Y. Q.; Yan, Z. K.; You, W. B.; Men, Q. Q.; Chen, G. Y.; Lv, X. W.; Wu, Y. Y.; Luo, K. C.; Zhao, B.; Zhang, J. C. et al. Balancing MXene surface termination and interlayer spacing enables superior microwave absorption. *Adv. Funct. Mater.* **2023**, *33*, 2301449.
[75] Chen, F.; Zhang, S. S.; Ma, B. B.; Xiong, Y.; Luo, H.; Cheng, Y. Z.; Li, X. C.; Wang, X.; Gong, R. Z. Bimetallic CoFe-MOF@$Ti_3C_2T_x$ MXene derived composites for broadband microwave absorption. *Chem. Eng. J.* **2022**, *431*, 134007.
[76] Zhou, X. D.; Zhang, H. B.; Yuan, M. Y.; Li, B. X.; Cui, J. C.; Qian, Y. T.; Liu, Y. H.; Yu, L. H.; Xiong, X. H.; Du, Y. Q. et al. Dispersing magnetic nanoparticles into staggered, porous Nano-frameworks: Weaving and visualizing nanoscale magnetic flux lines for enhanced

electromagnetic absorption. *Adv. Funct. Mater*., in press, https://doi.org/10.1002/adfm.202314541.

[77] Hou, X. W.; Wen, J. Y.; Wang, W. J.; Ye, W. P.; Zhang, Y.; Wang, S.; Cao, K. Y.; Zhao, R.; Xue, W. D. Electrostatic self-assembly hollow-VOOH/MXene composite for microwave absorption. *Compos. Commun.* **2023**, *41*, 101635.

[78] Chao, M.; Chu, N.; Zhang, B.; Luo, C. J.; Yan, L. K. MXene/carbon fiber/polyimide composite aerogel for multifunctional microwave absorption. *Compos. Commun.* **2024**, *46*, 101837.

[79] Wu, F.; Liu, Z. H.; Wang, J. Q.; Shah, T.; Liu, P.; Zhang, Q. Y.; Zhang, B. L. Template-free self-assembly of MXene and CoNi-bimetal MOF into intertwined one-dimensional heterostructure and its microwave absorbing properties. *Chem. Eng. J.* **2021**, *422*, 130591.

[80] Jiang, J.; Lan, D.; Li, Y. Q.; Yang, J.; Deng, S. L.; He, Q. C.; Wang, Y. Q. Construction of spherical heterogeneous interface on $ZnFe_2O_4$@C composite nanofibers for highly efficient microwave absorption. *Ceram. Int.* **2024**, *50*, 38331–38341.

[81] Cheng, Y. H.; Lan, D.; Jia, Z. R.; Gao, Z. G.; Liu, X. H.; Shi, X. T.; He, M. K.; Guo, H.; Wu, G. L. MOF derivatives anchored to multichannel hollow carbon fibers with gradient structures for corrosion resistance and efficient electromagnetic wave absorption. *J. Mater. Sci. Technol.* **2025**, *216*, 150–164.

[82] Li, S. S.; Zhu, M. Y.; Li, W.; Lu, Y. Z.; Tang, X. W.; Chen, H. J.; Wang, Z. X.; Xu, M. Y.; Li, Y.; Hu, Z. Y. et al. Hierarchical polyimide-based composite foam for compatible multi-band stealth. *J. Mater. Sci. Technol.* **2025**, *215*, 315–326.

[83] Qiao, J.; Song, Q. H.; Xuan, L. X.; Liu, J. R.; Zhang, X.; Zheng, S. N.; Lin, J. P.; Cai, W. Q.; Zhang, Q. D.; Zeng, Z. H. et al. Dual cross-linked magnetic MXene aerogel with high strength and durability enables multifunctionality. *Adv. Funct. Mater.* **2024**, *34*, 2401687.

[84] Zhao, X.; Tang, X. W.; Qiao, Y. L.; Li, S. S.; Zhang, Z. H.; Lu, Y. Z.; Zhu, M. Y.; Hu, Z. Y.; Long, L. J.; Wang, Z. C. et al. Ultrathin polyimide-based composites with efficient low-reflectivity electromagnetic shielding and infrared stealth performance. *Nano Res.* **2024**, *17*, 6700–6712.

[85] Wang, J. F.; Shen, M. M.; Liu, Z. X.; Wang, W. J. MXene materials for advanced thermal management and thermal energy utilization. *Nano Energy* **2022**, *97*, 107177.

[86] Ding, R. J.; Yan, Q.; Xue, F. H.; Li, P. Y.; Xiong, J. H.; Zhao, X.; Liu, Z. L.; Xu, L. L.; Chen, Z.; Zheng, H. W. et al. Dual protective porous $Ti_3C_2T_x$ MXene/polyimide composite film for thermal insulation and electromagnetic interference shielding. *Small* **2023**, *19*, 2304946.

[87] Gu, W. H.; Tan, J. W.; Chen, J. B.; Zhang, Z.; Zhao, Y.; Yu, J. W.; Ji, G. B. Multifunctional bulk hybrid foam for infrared stealth, thermal insulation, and microwave absorption. *ACS Appl. Mater. Interfaces* **2020**, *12*, 28727–28737.